Magnetic structure of bixbyite α-Mn_{2}O_{3}: A combined DFT+U and neutron diffraction study

Eric Cockayne, Igor Levin, Hui Wu, and Anna Llobet

Phys. Rev. B **87**, 184413 — Published 15 May 2013

DOI: 10.1103/PhysRevB.87.184413

The magnetic structure of bixbyite α-Mn_2O_3: a combined density functional theory DFT+U and neutron diffraction study

Eric Cockayne[1], Igor Levin[1], Hui Wu[1,2], and Anna Llobet[3]

[1]*National Institute of Standards and Technology, Gaithersburg, Maryland 20899 USA*

[2]*Department of Materials Science and Engineering, University of Maryland, College Park, Maryland 20742 USA and*

[3]*Lujan Neutron Scattering Center, Los Alamos National Laboratory, Los Alamos, NM 87545 USA*

Abstract

First principles density functional theory DFT+U calculations and experimental neutron diffraction structure analyses were used to determine the low-temperature crystallographic and magnetic structure of bixbyite α-Mn_2O_3. The energies of various magnetic arrangements, calculated from first principles, were fit to a cluster-expansion model using a Bayesian method that overcomes a problem of underfitting caused by the limited number of input magnetic configurations. The model was used to predict the lowest-energy magnetic states. Experimental determination of magnetic structure benefited from optimized sample synthesis, which produced crystallite sizes large enough to yield a clear splitting of peaks in the neutron powder diffraction patterns, thereby enabling magnetic-structure refinements under the correct orthorhombic symmetry. The refinements employed group theory to constrain magnetic models. Computational and experimental analyses independently converged to similar ground states, with identical antiferromagnetic ordering along a principal magnetic axis and secondary ordering along a single orthogonal axis, differing only by a phase factor in the modulation patterns. The lowest-energy magnetic states are compromise solutions to frustrated antiferromagnetic interactions between certain corner-sharing [MnO_6] octahedra.

PACS numbers:

Introduction

Manganese is a multivalent element. Each valence state has a characteristic oxide or oxides. Mn ion magnetism and electron correlations of Mn d states make it challenging to accurately determine the electronic structure of Mn oxides using the density functional theory (DFT) approach. Franchini *et al.*[1] explored various manganese oxides using DFT and showed that the electronic structure as well as the magnetic ground state depend sensitively on the details of the DFT calculation, such as the exchange-correlation functional used.

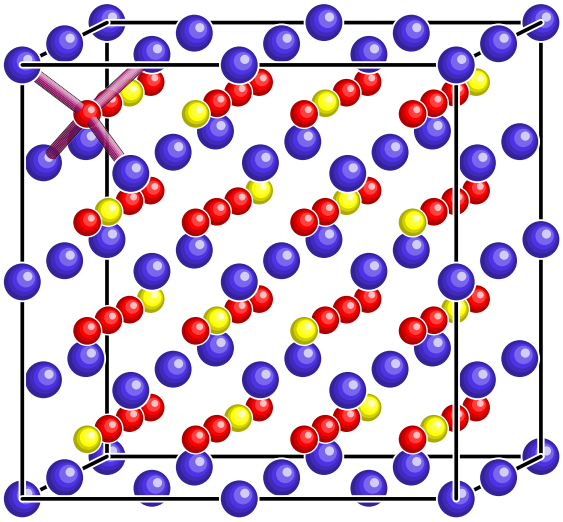

FIG. 1: Topology of bixbyite phase. Mn in dark blue; O in medium red; unfilled tetrahedral interstitials indicated in light yellow. The four nearest Mn to a given O are drawn in the upper left.

The α-Mn_2O_3 phase, with the bixbyite structure, is particularly challenging to model because of its complicated, and not yet completely solved, magnetic structure. In the bixbyite structure (Fig. 1), the Mn^{3+} ions are octahedrally coordinated, while the O ions have 4 Mn neighbors. The bixbyite structure can be viewed as a close-packed lattice of Mn with O ions filling 3/4 of the tetrahedral interstitials in a pattern with $Ia\overline{3}$ symmetry. Below about 300 K, α-Mn_2O_3 transforms from cubic to an orthorhombic structure with $Pbca$ symmetry[2]. The rhombohedral distortion increases with decreasing temperature, with lattice parameters at 81 K approximately a= 9.41 Å, b = 9.45 Å, and c = 9.37 Å (Refs. 2–4). Geller[5] rationalized the low-temperature orthorhombic distortion of bixbyite as a consequence of a Jahn-Teller instability of [MnO_6] octahedra toward elongation along any one of the three Cartesian axes.

In the cubic bixbyite phase, 24 of 32 Mn atoms exhibit distorted coordination whereas the remaining 8 Mn atoms, which occupy fixed-coordinate high-symmetry positions, retain regular coordination environments. The orthorhombic phase accommodates Jahn-Teller distortion of the remaining 8 octahedra (see Fig. 2-Fig. 3).

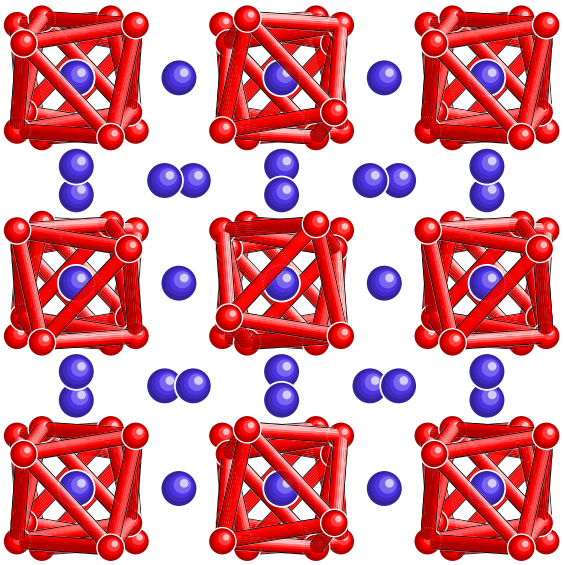

FIG. 2: Cubic α-Mn_2O_3 viewed along c axis; regular octahedra surrounding high-symmetry Mn sites shown, in columns with two octahedra per repeat unit along c. Blue balls are Mn; red balls O.

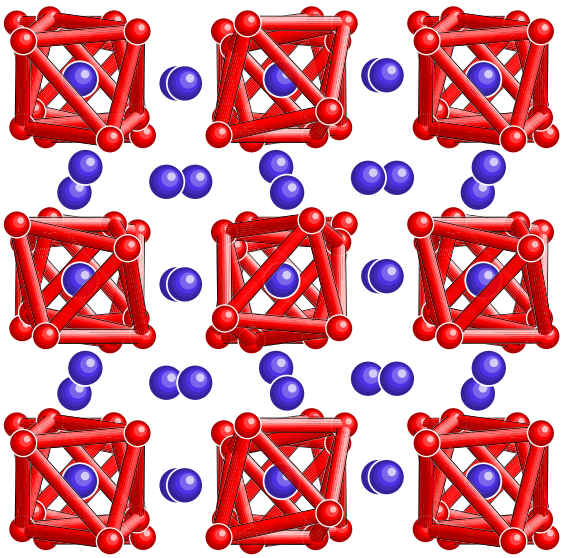

FIG. 3: Orthorhombic α-Mn_2O_3: octahedra shown in Fig. 2 have undergone Jahn-Teller distortion.

The magnetic structure of Mn_2O_3 has long been of interest, but it is not completely solved. Computationally, Franchini *et al.* found a preference for either antiferromagnetic or ferromagnetic ordering in α-Mn_2O_3, depending on the type of DFT exchange-correlation functional used[1]. Experimentally, Regulski *et al.*[6] found evidence for various antiferromagnetic ordering transitions within the orthorhombic phase, which occur without any apparent change in symmetry.

Grant *et al.*[7] suggested that the magnetic ordering of orthorhombic α-Mn_2O_3 can be predicted from the cubic $Ia\overline{3}$ symmetry because the orthorhombic distortion is small. They proposed a non-collinear ordering model with magnetic moments on the Mn 8(b) sites (4(a) and 4(b) in $Pbca$) aligned with the body diagonals of the pseudo-cubic cell and those on the Mn 24(d) sites (8(c) in $Pbca$) directed perpendicular to one of the two orthogonal 2_1 screw axes passing through each 24(d) site. However, Regulski *et al.* demonstrated that this model is incompatible with the neutron powder diffraction data[6]. They further identified an alternative, better-fitting, collinear model which featured antiferromagnetic ordering on each of the five inequivalent Mn sublattices of the orthorhombic structure. However, the orthorhombic distortion could not be resolved in the diffraction patterns used by Regulski *et al* and, therefore, the atomic positions had to be refined according to the high-temperature cubic $Ia\overline{3}$ structure. No refinements of the nuclear and magnetic structures of the magnetic phase under the correct orthorhombic symmetry have been reported.

In this paper, we address deficiencies in both the computational and experimental studies of the magnetic ground state of α-Mn_2O_3. Computationally, we use density functional theory at the DFT + U + J level in concurrence with a cluster-expansion model to investigate candidate ground state models until the correct DFT ground state is established. Experimentally, we use optimized conditions to synthesize α-Mn_2O_3 with crystallite sizes large enough to yield visible splitting of reflection peaks in the neutron diffraction patterns of the orthorhombic phase, and thus refine the magnetic ordering within orthorhombic symmetry. Both approaches give very similar results for the magnetic ordering, suggesting that the ground state magnetic structure of α-Mn_2O_3 is largely solved.

Computational Methods

First principles density functional theory (DFT) calculations, as encoded in the VASP software[8,9], were used to calculate the relaxed configurations investigated here and their electronic structures. The generalized gradient approximation (GGA) for the exchange-correlation functional was used throughout, within the "Perdew-Burke-Ernzerhof revised for solids" or "PBEsol" parameterization[10].

The PBEsol exchange-correlation functional has been found to give excellent results compared with experiment for the lattice parameters and bulk moduli of both metals and nonmetals[11]. As is generally true for DFT, however, calculated band gaps are too small. This error can lead to qualitative errors for narrow bandgap materials and for materials with magnetic ions, both which are true for α-Mn_2O_3. We compensated for this error by including onsite Coulomb terms (the "GGA+U" approximation). In a previous study of MnO_2 phases[12], we found that the experimental volume and bandgap of β-MnO_2 could both be reproduced using the rotationally invariant DFT+U of Liechtenstein *et al.*[13] with an onsite Coulomb parameter $U = 2.8$ eV and onsite exchange parameter[14] $J = 1.2$ eV for Mn d electrons. Remarkably, these same values used for the Mn^{4+} ion of β-MnO_2 ion were found to be transferable to the Mn^{3+} ion of α-Mn_2O_3, giving excellent agreement with experiment, as shown below. *Ex post facto* investigations of the effects of varying the Mn U and J parameters, or adding U or J parameters for oxygen, gave little, if any, improvement.

Sufficient convergence in total energies and lattice parameters was achieved with a plane wave cutoff energy of 500 eV and a 2×2×2 Monkhorst-Pack grid of k-points. A 8×8×8 Monkhorst-Pack grid was used for density of states calculations. The magnetic ordering of each of the 32 Mn atoms in the unit cell could be set either "up" or "down" as desired. Spin-orbit coupling was neglected. Only collinear magnetic structures were computed using VASP.

The aim of the computational work was to find the DFT ground state magnetic ordering of α-Mn_2O_3. The cluster-expansion concept, as developed for interatomic alloys[15,16], was used to identify candidate states to explore. The formal mathematics of the spin-state problem is identical to that of the alloy problem. Each site i is given a parameter σ_i, where $\sigma_i = 1$ for spin up (species A in the alloy problem) and $\sigma_i = -1$ for spin down (species B in the alloy problem).

The total energy U of a configuration $\{\sigma_i\}$ is written as

$$U(\{\sigma_i\}) = \sum_\alpha J_\alpha \xi_\alpha, \tag{1}$$

where α are the symmetry distinct geometric clusters, J_α the effective spin interaction parameter for cluster α, and ξ_α the average spin product over all symmetry equivalent occurrences of this cluster[17].

In practice, one calculates individual U for various configurations, determines the values of the J_α according to some fitting procedure, and then uses these values to estimate the energies of any configuration, including those that are not part of the fit. Errors in the determination of the J_α due to the finite set of included energies lead to errors in the predictions. While any method for determining the J_α should eventually converge to the same result given a sufficiently large number of input configurations, in this work, we employ the cluster expansion method formulated by Cockayne and van de Walle[18]. This method uses DFT results to fit a number of J_α parameters that is much *larger* than the number of results. The mathematical problem of overfitting the data (that is, the non-uniqueness of the solution) is controlled using a Bayesian approach[18,19]. A physically motivated probability distribution of all J_α values is the Bayesian prior. The DFT results are a series of constraints used to update the probability distribution via Bayes' Theorem. The posterior distribution of the J_α gives the most probable values of the J_α and their standard deviations. Additionally, the method of Ref. 18 reproduces all of the DFT energies used to generate the cluster expansion *exactly*, and gives self-consistent error estimates for all predictions.

All results were calculated within an identical 80-atom, 32 Mn cell. The cluster interactions that can be determined are limited to those contained within one unit cell. The model is valid for predictions of other configurations within the same cell, but can not be applied to larger supercells; thus if the ground state magnetic state has a larger periodicity than the crystallographic one, it will be missed.

There are 2^{32} collinear magnetic states for the 32 Mn atoms in the α-Mn_2O_3 unit cell. Time reversal and crystallographic symmetry reduce the number of symmetry-independent configurations to about $3\times\ 10^8$, which, according to a one-to-one correspondence with the number of cluster terms[15,20], yield about $3\times\ 10^8$ unknown cluster terms. Solving linear sets of equations with order 10^8 unknowns is not computationally feasible. To simplify the problem, we truncated the interaction terms at fourth order (time reversal symmetry forbids

linear or cubic terms in the magnetic interactions). There is 1 constant term, 73 independent pair cluster term and 4632 four-body cluster terms in our model. For sets of n DFT total energy results, we solved n equations in 4706 unknowns, using a Bayesian prior to weight the parameters and standard singular value techniques for solving underdetermined sets of linear equations.

The prior that we used for the pair terms was

$$P = \prod_{ij} \exp(-J_{ij}^2/(2w_{ij}^2)), \tag{2}$$

with

$$w(i,j) = A\big(\frac{d_0}{d_{ij}}\big)^2, \tag{3}$$

where d_{ij} is the distance between the Mn at site i and j and $d_0 \approx 3.3$ Å$= \sqrt{2}a_0/4$ is the approximate nearest-neighbor Mn-Mn distance and A is an unknown constant. The prior for the four-body terms was of similar form, with

$$w(i,j,k,l) = A\big(\frac{d_0}{d_{ij}}\big)^2\big(\frac{d_0}{d_{ik}}\big)^2\big(\frac{d_0}{d_{il}}\big)^2\big(\frac{d_0}{d_{jk}}\big)^2\big(\frac{d_0}{d_{jl}}\big)^2\big(\frac{d_0}{d_{kl}}\big)^2 \tag{4}$$

The physical motivation behind the form of this interaction was to weaken cluster terms involving Mn ions that are farther apart from each other. Although superexchange spin interactions are short range, we expect that strain coupling effects may mediate longer range interaction; thus the $(d_{ij})^{-2}$ form for our relative interaction terms in the prior. The value of A was determined self-consistently by the leave-one-out cross validation method[18]. This value was scaled such that the root mean square error in the predicted energies equalled the root mean square of the predicted errors[18].

We studied the magnetic states in an iterative manner. After calculating an initial set of energies versus magnetic orderings for a few simple configurations, additional structures were investigated, with, in rotating turns, (1) the minimum predicted energy among untested structures, (2) the maximum predicted energy among untested structures, and (3) the maximum predicted uncertainty in energy. The parameters J_α were recalculated after each step, and then used to predict the energies and energy uncertainties for *all* order 3×10^8 symmetry independent configurations. The model was refined iteratively until there were no more predicted states within two standard deviations of uncertainty of the tenth lowest-energy state found, at which point it was concluded that the collinear ground state was probably found. 76 structures in all were calculated.

Experimental Methods

The α-Mn_2O_3 powder sample was prepared by heating $MnCO_3$ (analytical reagent) at 800 °C in air for 12 h, which was the highest temperature to yield phase-pure α-Mn_2O_3 devoid of Mn_3O_4 traces. The sample was characterized using X-ray powder diffraction in an instrument equipped with an incident-beam monochromator (Cu $K_{\alpha 1}$ radiation) and a position sensitive detector. The heating temperature and time were selected to minimize the width of the 222 peak, which remains non-split in the orthorhombic phase and, therefore, reflects the size of the coherently scattering domains in the sample. (Phase-pure α-Mn_2O_3 can be obtained by heating $MnCO_3$ at temperatures between 600 °C and 800 °C, but lower temperatures produced considerably broader peaks). No changes in the peak widths were observed after the second heating at 800 °C for 12 h.

Neutron powder diffraction measurements were performed using both the time-of-flight HIPD diffractometer at the Lujan Center of the Los Alamos National Laboratory and the BT-1 constant-wavelength (Cu 311 monochromator, $\lambda = 1.5405$ Å, 15' collimation) diffractometer at the NIST Center for Neutron Research. For these measurements, the α-Mn_2O_3 powder was loaded in vanadium cans. In each experiment the data were collected at a series of temperatures (HIPD: 300 K, 200 K, 150 K, 100 K, 60 K, 40 K, 5 K and BT-1: 300 K, 100 K, 40 K, 10 K, 2 K). Rietveld refinements of the nuclear and magnetic structures were performed using GSAS[21].

The magnetic-structure models were selected according to representational analyses performed by SARAh[22]; likewise, SARAh was used for symmetry-constrained refinements in GSAS. First, the magnetic basis-vector coefficients were refined using a Reverse Monte Carlo (RMC) algorithm implemented in SARAh with the magnitudes of all the magnetic moments constrained to be equal. The best-fit model was further refined in GSAS (i.e. using least squares minimization) by keeping the basis-vector coefficients fixed but allowing for distinct ordered magnetic moments on inequivalent Mn sites. The HIPD and BT-1 data produced consistent structural parameters.

TABLE I: DFT crystal structure for ferromagnetic α-Mn_2O_3 in cubic $Ia\overline{3}$ phase. Lattice constant $a_0 = 9.4090$ Å.

Species	Site	x	y	z
Mn(1)	8(a)	0	0	0
Mn(2)	24(b)	0	1/4	0.2848
O(1)	24(b)	0.4162	0.1286	0.3555
O(2)	24(b)	0.3714	0.1445	0.0838

Computational Results

The α-Mn_2O_3 bixbyite structure was first investigated with ferromagnetic ordering. Relaxation under cubic $Ia\overline{3}$ symmetry, yielded $a_0 = 9.409$ Å, and the structure shown in Table I. DFT phonon results of this cubic structure show an extremely strong double instability ($\nu = 510\ i\ \mathrm{cm}^{-1}$), associated with Jahn-Teller distortions of the oxygen octahedra centered on the Mn(1) sites. Full relaxation of the bixbyite structure perturbed by either mode in the instability doublet, or any linear combination of the two, leads to an orthorhombic minimum energy state with *Pbca* symmetry, explaining the experimental cubic-orthorhombic transition. In fact, we find that all such combinations relax to the *same* ferromagnetic ground state structure, differing only with respect to (1) which of the original cubic axis becomes the short axis of the orthorhombic unit cell and (2) possible translations of the origin by (1/2,1/2,1/2). Each Mn(1) and Mn(2) in the orthorhombic structure has four short Mn-O distances and two long Mn-O distances. The topology of the orthorhombic structure is uniquely defined by specifying which Mn(1)-O and Mn(2)-O distances are long. In this work, we arbitrarily choose the setting where the Mn(1) at (0,0,0) has its far O neighbors at approximately $\pm(0.139, 0.149, -0.093)$, and the Mn(2) at (1/2,1/2,1/2) has its far O neighbors at approximately $\pm(0.656, 0.412, 0.641)$. The ground state ferromagnetic structure is shown in the left-hand side of Table II.

The orthorhombic crystallographic structure of the ferromagnetic phase was used as the starting part for relaxation of each collinear spin combination $\{\sigma_i\}$ studied. The state that was ultimately identified as the ground state was the 36th studied. In total, 76 states were investigated before the termination criterion was reached: no new structures with predicted

TABLE II: DFT crystal structures for orthorhombic ferromagnetic and ground state antiferromagnetic structures. The similarity of a and b for the orthorhombic ferromagnetic structure is coincidental[23].

		FM			AFM ground		
a		9.4417			9.4024		
b		9.4417			9.4435		
c		9.4096			9.3668		
Atom	Site	x	y	z	x	y	z
Mn(1)	4(a)	0	0	0	0	0	0
Mn(2)	4(b)	1/2	1/2	1/2	1/2	1/2	1/2
Mn(3)	8(c)	0.2563	0.2854	-0.0070	0.2602	0.2848	-0.0102
Mn(4)	8(c)	0.2864	-0.0010	0.2458	0.2857	-0.0034	0.2450
Mn(5)	8(c)	0.0079	0.2478	0.2845	0.0136	0.2457	0.2818
O(1)	8(c)	0.4215	0.1259	0.3510	0.4256	0.1233	0.3502
O(2)	8(c)	0.1358	0.3523	0.4103	0.1409	0.3506	0.4050
O(3)	8(c)	0.3576	0.4180	0.1223	0.3568	0.4187	0.1196
O(4)	8(c)	0.0855	0.3721	0.1414	0.0845	0.3738	0.1395
O(5)	8(c)	0.3791	0.1460	0.0794	0.3815	0.1478	0.0798
O(6)	8(c)	0.1524	0.0859	0.3648	0.1567	0.0873	0.3608

energies within two standard deviations of the tenth-lowest-energy structure found.

The calculated ground state collinear magnetic structure is shown in Fig. 4 and listed in Table III. The spin moments are obtained by taking the difference in the number of spin up and spin down electrons, integrated within spheres of radius 1.24 Å centered on each Mn, as calculated using VASP. The magnitudes are reasonable for high-spin Mn^{3+} ions, but are not precisely comparable with experiment because of the artificial partition of the cell into spherical volumes.

We next investigated possible noncollinear magnetism using the parameters found in the fit to the computational results. The obvious way to extend the model is to use the interaction parameters determined from calculations of collinear systems with (pseudo)vectorized

TABLE III: Ground state DFT magnetic state and lowest energy noncollinear magnetic state found in a Heisenberg model based on pair interactions determined by fits to DFT results. Units are μ_B. Only the relative directions of the magnetic moments are determined; $m_\parallel$ is the magnetic moment along the only axis for the collinear DFT ground state and principal axis of the noncollinear Heisenberg model ground state; $m_\perp$ is the magnet moment along a second axis of the Heisenberg model ground state. Mn positions as in Table II; spin moments for other Mn are related by applying the factors shown in Table IV.

	DFT	Heisenberg		
Atom	$m_\parallel$	$m_\parallel$	$m_\perp$	ϕ
Mn(1)	-3.6	-3.6	0.0	0
Mn(2)	-3.6	-3.6	0.0	0
Mn(3)	3.6	3.0	-1.9	32
Mn(4)	3.6	3.2	1.6	27
Mn(5)	-3.6	-3.6	-0.1	1

TABLE IV: Effects of *Pbca* symmetry generators on the magnetization components of the theoretical α-Mn_2O_3 magnetic structures listed in Table III.

Generator	$m_\parallel$	$m_\perp$
(x,1/2-y,1/2+z)	-1	-1
(1/2+x,y,1/2-z)	-1	-1
(1/2-x,1/2+y,z)	+1	-1

spins in a Heisenberg model approach. That is, instead of using Ising-like interaction terms $J_{ij}\sigma_i\sigma_j$, one uses Heisenberg-like interaction of spin "vectors" according to the principle axes of "up" spin: $J_{ij}\vec{\sigma}_i \cdot \vec{\sigma}_j$, with exactly the same set of J_{ij} (note that the posterior likelihood of coupling parameters J_α is actually a *distribution*, in the following, we use only the *most probable* set of values for the J_α). For simplicity, we only included pair interactions in this approach[24]. Simulated annealing was used to find the lowest energy state of the Heisenberg model. Random initial spin configurations always converged to an equivalent noncollinear ground state (right side of Table III), with a dominant spin axis direction $m_\parallel$, and all secondary spin components along the same orthogonal axis $m_\perp$.

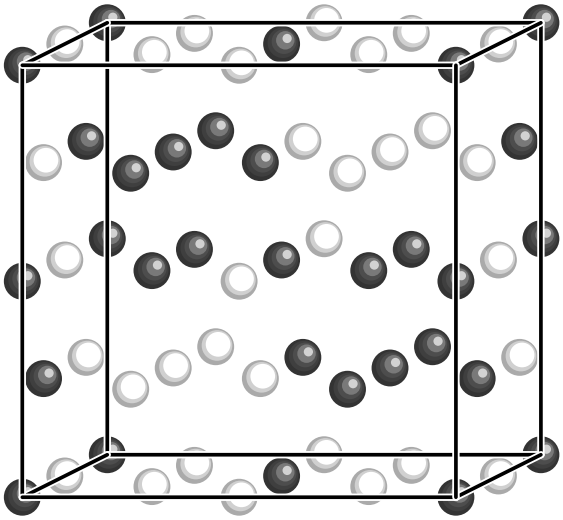

FIG. 4: Lowest-energy collinear magnetic structure found computationally; also collinear model that gives best fit ($\chi^2 = 2.54$) to experimental results at 2 K. Only Mn atoms shown; dark spheres represent spin "up" and light spheres spin "down".

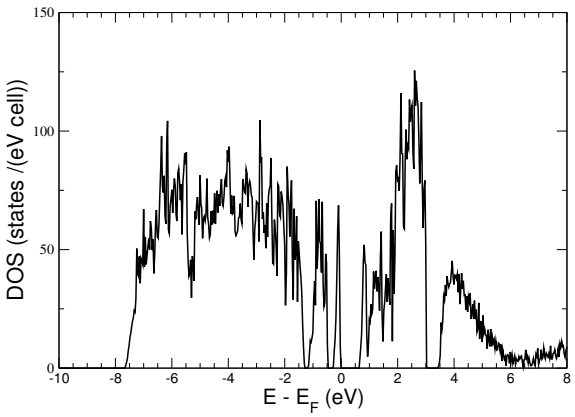

FIG. 5: Calculated density of states (DOS) for α-Mn_2O_3 in ground state collinear magnetic structure.

The band structure for the lowest-energy collinear magnetic state found is shown in Fig. 5. The structure has some similarities to that of Franchini *et al.*[1], using the PBE0 approximation, including a band gap at the Fermi level (0.6 eV in our case). Our results differ from theirs in that our antiferromagnetic structure (as opposed to their ferromagnetic structure) results in a band structure without a global distinction between majority and minority spins. Locally, around the magnetic Mn sites, one spin direction dominates. In Fig. 6, we show the integrated DOS around each distinct Mn site, broken down into majority

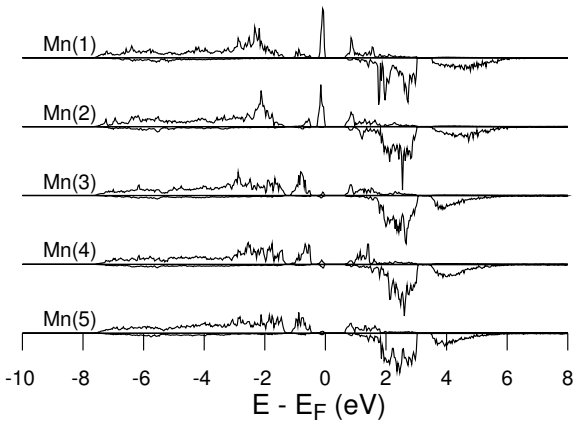

FIG. 6: Integrated density of states (DOS) for α-Mn_2O_3 in ground state collinear magnetic structure, within spheres of radius 1.24 Å centered on each Mn site. Integrated DOS of local majority spins above the line and local minority spins below the line.

and minority spins. We find a remarkable signature of the combination of octahedral crystal field splitting and effects of Jahn-Teller distortion in the nature of the highest occupied levels: they are split off from the other occupied $3d$ states. The highest valence band is an isolated band associated with $3d$ electrons of the Mn(1) and Mn(2). A second split band at around $E_F - 0.8$ eV is associated with Mn(3), Mn(4), and Mn(5) $3d$ electrons (Fig. 6).

Experimental Results

Room-temperature diffraction patterns (Fig. 7) exhibit no clear reflection splitting indicative of an orthorhombic distortion. However, the peaks are broad and the cubic $Ia\overline{3}$ model fits poorly yielding abnormally large atomic displacements parameters U_{iso} for the oxygen atoms, which suggests that the structure is distorted. The data (not shown) can be fitted satisfactorily using the orthorhombic *Pbca* structure reported in the literature with sensible U_{iso} values. The refined lattice distortion at 300 K differed considerably between the HIPD data ($b/c = 1.0007$) and BT-1 data ($b/c = 1.0036$), presumably because of the close proximity of the phase transition which leads to relatively large changes in the lattice distortion even for small temperature differences. The distortion increases rapidly on cooling to $b/c = 1.0085$ at 100 K and the reflection splitting becomes evident (Fig. 7). For these temperatures, the lattice parameters refined using the HIPD and BT-1 data were in good agreement. Temperature dependencies of the lattice parameters, unit cell volume, and b/c

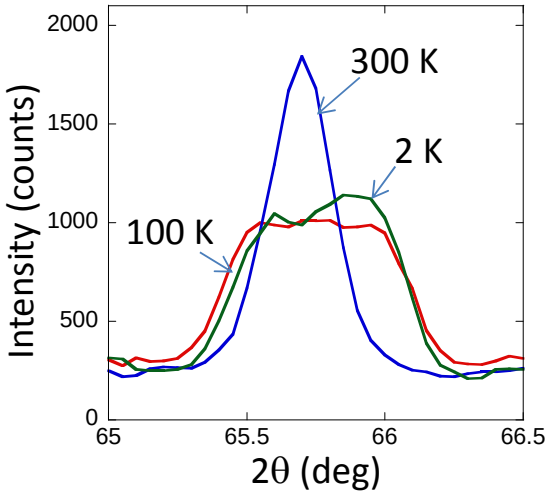

FIG. 7: A trace of the 622 cubic reflection at three different temperatures. This reflection appears as a single peak at 300 K but exhibits pronounced splitting at sub-ambient temperatures. Similar trends are observed for other reflections.

data are summarized in Fig. 8. Fig. 9 displays the experimental and calculated diffraction profiles for T=100 K, while Table V summarizes the results of the nuclear-structure refinements at 100 K and 2 K. The MnO_6 octahedra exhibit strong Jahn-Teller distortions already at 300 K (Table VI).

Below 100 K, a series of strong reflections appears at lower angles, which signifies magnetic ordering (Fig. 10). The b/c ratio decreases slightly below the magnetic transition (Fig. 8(b)) to 1.0079 at 2 K. The patterns remain qualitatively unchanged from 60 K down to 2 K. The magnetic reflections can be accounted for by a propagation vector k=0. All eight symmetry elements of the space group *Pbca* leave this propagation vector invariant. Group-theory analysis yields eight irreducible representations (IR) (Γ_i, i=1, 8), each having an order of one. Only four of these IRs (Γ_1, Γ_3, Γ_5, and Γ_7), are common to all five of the inequivalent Mn sites.

Regulski *et al.*[6] presented their collinear magnetic-ordering model in the form of schematic drawings for each Mn sublattice; no symmetry analysis was performed. According to our representational analysis, the ordering types for their sublattices 1 (combined Mn 4(a) and 4(b) sites), 2, and 4 belong to the Γ_3 representation. However, the ordering on their sublattice 3 is incompatible with any of the IRs; that is, the model, at least as presented, is not compatible with orthorhombic crystallographic symmetry (possibly there is a drawing

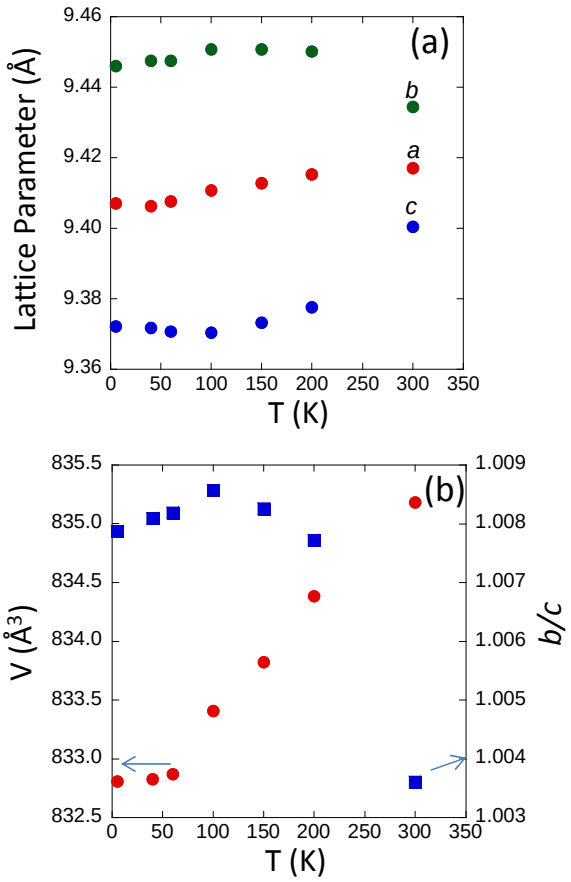

FIG. 8: Temperature dependence of the (a) orthorhombic lattice parameters and (b) unit-cell volume and b/c ratio which characterizes the magnitude of the orthorhombic distortion. The behavior of the orthorhombic distortion changes across the magnetic transition at approximately 80 K. The error bars are within the size of the symbols.

error). The spin arrangement for their sublattice 3 can be made compatible with the structural symmetry by flipping the directions of two spins. The resulting ordering patterns belong to either the Γ_3 or Γ_6 representations, depending on which two spins are flipped. We fitted both models (*i.e.* Γ_3 and $\Gamma_3 + \Gamma_6$) to our data. A collinear pattern with magnetic moments directed along one of the orthorhombic axes was assumed. The Γ_3 model with all the moments parallel to the c-axis produced a superior fit of quality comparable to that reported by Regulski *et al.* However, examination of the misfit between the calculated and experimental profiles reveals significant discrepancies for several magnetic reflections that become split in the orthorhombic structure (Fig. 10(a)), which indicates that the intensity distribution among the split-peak components is incorrect. Conceivably, these deficiencies

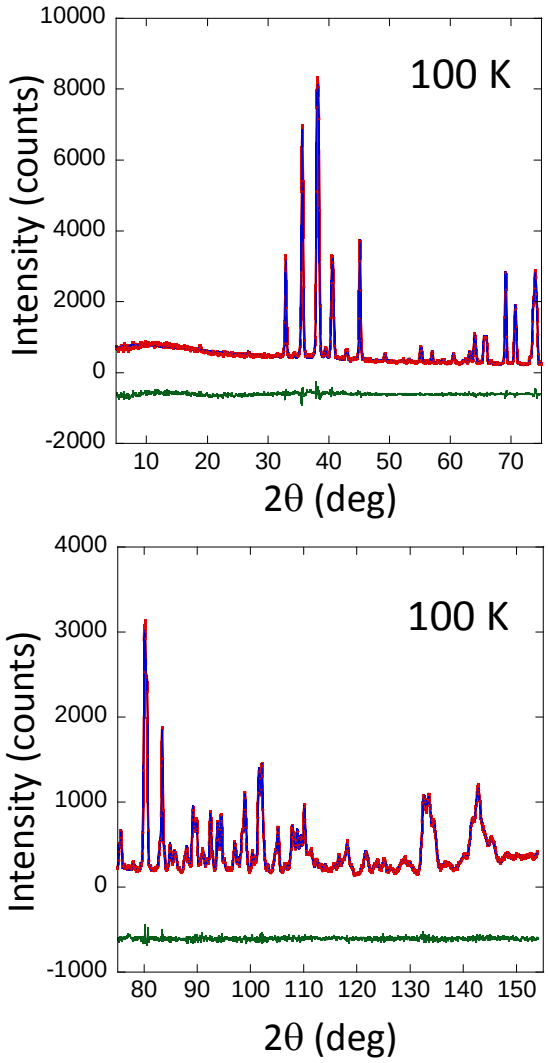

FIG. 9: Experimental (red/dots) and calculated (blue/line) neutron diffraction profiles (BT-1) for α-Mn_2O_3 at 100 K. The residual is indicated below (green line). The agreement factors are $\chi^2 = 1.16$ and $R_{wp} = 4.79\%$.

were obscured by the insufficient resolution in the data used by Regulski *et al.*

As the literature model failed to describe the data, we considered collinear models corresponding to other representations (i.e. Γ_1, Γ_5 and Γ_7). The Γ_1 model with the magnetic moments directed along the a-axis provided a satisfactory fit to the neutron data of quality far superior to that obtained for any of the Γ_3 models (Fig. 10(b)); the collinear Γ_1 models with magnetic moments directed along the b and c-axes yielded considerably worse agreement factors. Models generated according to the Γ_5 and Γ_7 representations generated poor fits and were discarded. Refinements of the magnetic-moment magnitudes (m) indepen-

TABLE V: Parameters of the nuclear structures of paramagnetic (T=100 K) and antiferromagnetic (T=2 K) α-Mn_2O_3 obtained by Rietveld refinements using neutron powder diffraction data (BT-1). In both cases, the space group is *Pbca* (#61). The model assumed isotropic atomic displacement parameters (U_{iso}), which were constrained according to the atom type (i.e. Mn or O). The refined values were U_{iso}(Mn) = 0.0031(2) Å^2 and U_{iso}(O) = 0.0049(1) Å^2 at 100 K and U_{iso}(Mn) = 0.0021(3) Å^2 and U_{iso}(O) = 0.0040(1) Å^2 (O) at 2 K. Numbers in parentheses refer to one standard deviation as calculated in GSAS.

		100 K ($\chi^2 = 1.16$)			2 K ($\chi^2 = 2.54$)		
a		9.4104(1)			9.4078(1)		
b		9.4509(1)			9.4488(1)		
c		9.3706(1)			9.3739(1)		
Atom	Site	x	y	z	x	y	z
Mn(1)	4(a)	0	0	0	0	0	0
Mn(2)	4(b)	1/2	1/2	1/2	1/2	1/2	1/2
Mn(3)	8(c)	0.2598(5)	0.2854(3)	-0.0105(5)	0.268(1)	0.280(1)	-0.011(1)
Mn(4)	8(c)	0.2867(3)	0.0017(8)	0.2436(4)	0.2880(9)	0.009(2)	0.246(1)
Mn(5)	8(c)	0.0127(5)	0.2456(6)	0.2827(3)	0.012(1)	0.237(1)	0.2833(9)
O(1)	8(c)	0.4253(3)	0.1241(4)	0.3511(4)	0.4276(8)	0.1240(9)	0.3502(8)
O(2)	8(c)	0.1399(3)	0.3509(4)	0.4068(2)	0.1395(8)	0.3513(9)	0.4074(7)
O(3)	8(c)	0.3579(3)	0.4175(4)	0.1218(3)	0.3586(9)	0.4169(9)	0.1209(7)
O(4)	8(c)	0.0838(3)	0.3725(4)	0.1402(3)	0.0738(7)	0.3712(9)	0.1385(9)
O(5)	8(c)	0.3797(3)	0.1477(4)	0.0789(3)	0.3821(8)	0.1509(9)	0.0803(7)
O(6)	8(c)	0.1554(3)	0.0882(3)	0.3609(4)	0.1563(8)	0.0882(9)	0.3586(8)

dently for each Mn site significantly improved the fit. The resulting m-values, which at 2 K range from approximately 3 μ_B to 4 μ_B, are consistent with those expected for Mn^{3+} ions. The collinear model most consistent with the experimental results is shown in Table VII. It is *identical* to that determined computationally (Fig. 4).

We explored potential deviations from the collinearity using the algorithms implemented in SARAh. A relatively large number of RMC cycles (3,000 for 2 basis-vector mixing coefficients per site and 10,000 for 3 coefficients per site) were found necessary to locate a model

TABLE VI: Mn-O distances at 300 K and 100 K (in Å). Numbers in parentheses refer to one standard deviation as calculated in GSAS.

	300 K		100 K	
Atom				
Mn(1)	2.03(2) (×2)		1.949(3) (×2)	
	2.02(1) (×2)		1.944(3) (×2)	
	1.97(2) (×2)		2.129(3) (×2)	
Mn(2)	2.04(2) (×2)		1.953(3) (×2)	
	1.90(1) (×2)		2.117(3) (×2)	
	2.04(2) (×2)		1.923(3) (×2)	
Mn(3)	2.17(2)	1.88(1)	2.200(5)	1.879(5)
	2.03(2)	2.31(2)	1.987(5)	2.327(5)
	1.92(1)	2.00(2)	1.915(5)	1.961(5)
Mn(4)	2.00(2)	2.20(2)	2.033(6)	2.181(7)
	1.90(1)	1.96(2)	1.934(5)	1.959(6)
	2.35(2)	1.88(1)	2.269(7)	1.859(5)
Mn(5)	1.90(2)	1.96(2)	1.889(5)	1.943(5)
	2.26(2)	1.91(2)	2.358(6)	1.916(5)
	1.98(2)	2.18(2)	2.026(5)	2.134(5)

that provides an adequate fit (a goodness-of-fit $\chi^2 \leq 3$) to the data. Detailed refinements of the magnetic structure were performed at 40 K and 2 K. Multiple refinements that start from randomly selected values of the mixing coefficients were run to verify the robustness of the best-fit structural model at 2 K.

The best fit was obtained by restricting the magnetic moments to the orthorhombic (010) plane. The fit of the several magnetic reflections was visibly improved in the non-collinear model (Fig. 10(c), Fig. 11). The best-fit Γ_1 models at both 40 K and 2 K feature similar patterns of magnetic ordering (Table V). No additional improvement was obtained by varying all three mixing coefficients per site after 20,000 RMC cycle; possibly, even this number of cycles was insufficient to identify a global minimum. In the best-fit non-collinear model, the magnetic moments are aligned preferentially with the a-axis but exhibit

TABLE VII: Magnetic-moment (m) components for the Mn atoms in the best-fit Γ_1 models at 2 K and 40 K. The atomic coordinates at 2 K are given in Table V. The magnetic-ordering model assumed m_y=0. The refined magnitudes of m (units of μ_B) are indicated for the inequivalent Mn sites. Magnetic moments for the remaining Mn sites are generated as described in Table VIII. The refinements at 2 K and 40 K were performed independently with the random starting models for the basis-vector mixing coefficients. The angle between the m_{tot} and the a-axis is defined as ϕ (°). Numbers in parentheses refer to one standard deviation as calculated in GSAS.

	2 K				40 K			
Atom	m_x	m_z	m_{tot}	ϕ	m_x	m_z	m_{tot}	ϕ
Mn(1)	-2.6	1.6	3.1(1)	32	-2.3	1.4	2.7(1)	32
Mn(2)	-3.4	-0.7	3.5(1)	12	-3.0	-0.8	3.1(1)	15
Mn(3)	3.2	-1.4	3.5(1)	23	3.0	-0.3	3.0(1)	5
Mn(4)	3.0	1.3	3.3(1)	24	2.9	0.3	2.9(1)	6
Mn(5)	-3.5	-2.3	4.2(1)	34	-3.4	-1.0	3.5(1)	16

TABLE VIII: Effects of generators of *Pbca* symmetry on magnetic moments refined experimentally.

Generator	m_x	m_z
(x,1/2-y,1/2+z)	-1	-1
(1/2+x,y,1/2-z)	-1	+1
(1/2-x,1/2+y,z)	+1	-1

significant (up to 32°) deviations from this direction; the deviations from collinearity become especially pronounced at 2 K.

Discussion

The theoretical lattice parameters of orthorhombic α-Mn_2O_3 change significantly when the magnetic structure changes from ferromagnetic to the antiferromagnetic lowest-energy collinear state (Table II), demonstrating significant spin-strain coupling. The ground state lattice parameters are within about 0.1% of experiment, phenomenally good agreement that demonstrates the accuracy of DFT calculations using the PBEsol exchange correlational

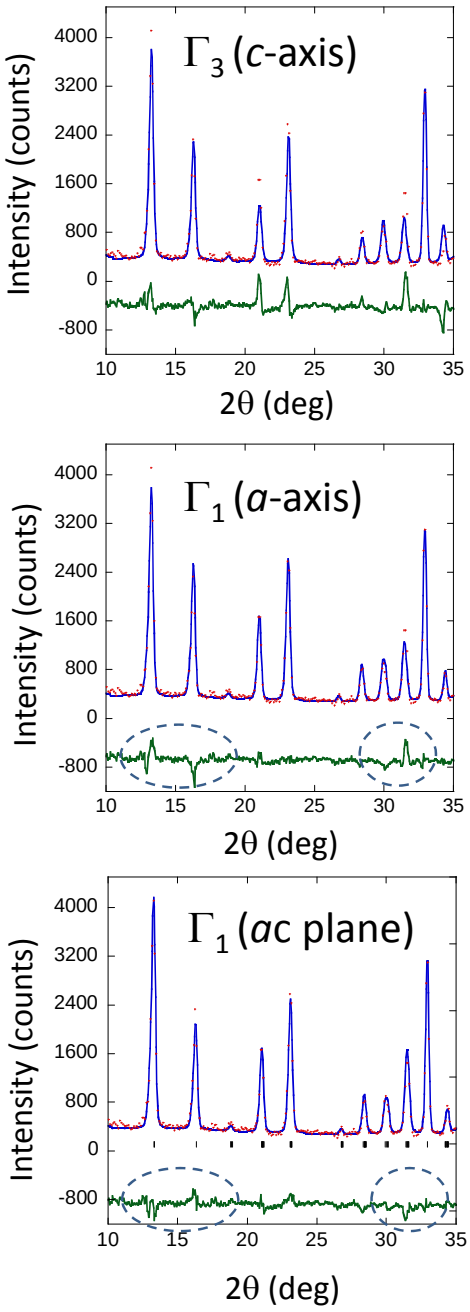

FIG. 10: A low-angle portion of the neutron diffraction pattern collected at 2 K showing experimental (red/dots) and calculated (blue/line) neutron diffraction profiles. Note that all the reflections with $2\theta \leq 32^\circ$ were absent at 100 K (Fig. 9); these reflections, all indexable according to the primitive nuclear-structure unit cell, originate from magnetic ordering. The calculated profiles correspond to (top) the Γ_3 model by Regulski et al. with magnetic moments aligned with the c-axis, (middle) the Γ_1 model with magnetic moments collinear with the a-axis, and (bottom) the Γ_1 model with non-collinear magnetic moments residing in the *ac* plane. The Γ_1 models provide a superior fit relative to the Γ_3 model. A non-collinear alignment of magnetic moments significantly improves the fit for several magnetic reflections (outlines using a dashed line).

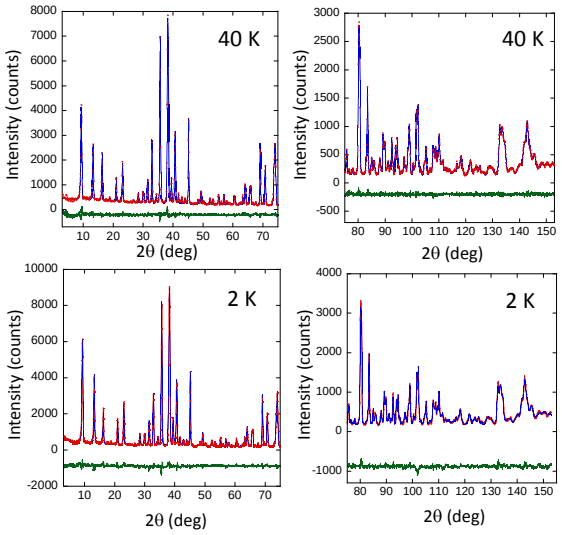

FIG. 11: Experimental (red/dots) and calculated (blue/line) neutron diffraction profiles (BT-1) for α-Mn_2O_3 at 40 K (top) and 2 K (bottom). The calculated profiles correspond to the Γ_1 model with the non-collinear array of magnetic moments in the ac plane. The agreement factors are $\chi^2 = 1.22$ and $R_{wp} = 5.21\%$ (40 K) and $\chi^2 = 2.53$ and $R_{wp} = 6.89\%$ (2 K).

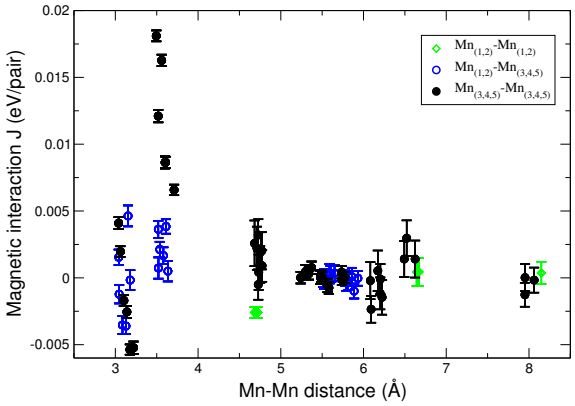

FIG. 12: Calculated magnetic interaction parameters between Mn ions in α-Mn_2O_3. Positive values for J favor antiferromagnetic alignment. Mn subscripts refer to the different Mn sites in the orthorhombic phase. Error bars indicate plus and minus one standard deviation of the parameter, based on cross-validation calculations.

along with on-site U and J parameters to treat d-electron correlations in Mn.

The lowest DFT collinear state found and the best low-temperature experimental fit to a collinear model are identical, although they were achieved completely independently, suggesting that the nature of the magnetism in α-Mn_2O_3 is largely solved. The secondary

components of the best noncollinear spin arrangements of model and experiment (Table III and Table VII) appear different at first glance, but in fact, the two are related by the approximate relationship $m_{\perp}(\text{model}) \approx \cos(2\pi x) m_{\perp}(\text{expt.})$, with x the crystallographic positional coordinate. The source of the discrepancy is not clear, but the agreement is noteworthy given the approximations involved in the computational approach. Note that the experimental results show clear preferences for magnetic moments along particular *directions*; the DFT approach neglected spin-orbit coupling, and thus the effect of magnetic moment direction could not be studied.

The experimental results (Table VII) for total magnetic moment per site, m_{tot}, are more variable than the computational values (Table III), which are similar for all Mn sites. As noted above, the theoretical moments are simply the differences in the number of spin up and spin down electrons within spheres of somewhat arbitrary radius 1.24 Å centered on each Mn; therefore the calculated moments are not directly comparable with the experimental values. Also, thermal spin fluctuations at 40 K decrease the experimentally measured m_{tot} from the values measured at 2 K and increase the differences in measured m_{tot} among the different Mn sites (Table VII). The values of the experimental and computed magnetic moments are reasonable for high-spin Mn^{3+} ions.

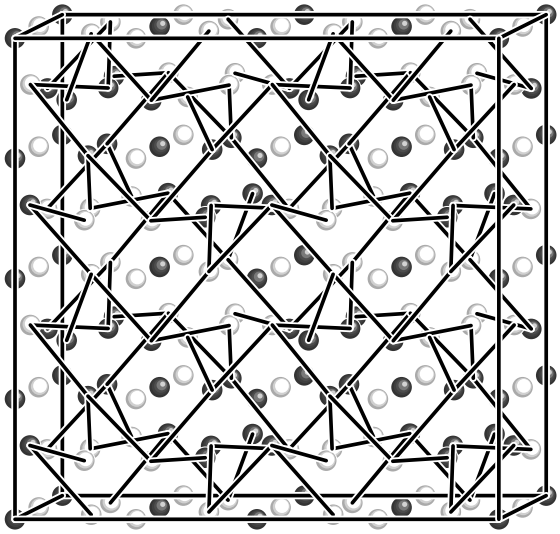

FIG. 13: Linkages between Mn in α-Mn_2O_3 limited to a subset of those with strong antiferromagnetic interactions as determined in this work gives the lowest energy collinear magnetic structure on the Mn(3), Mn(4), and Mn(5) sites.

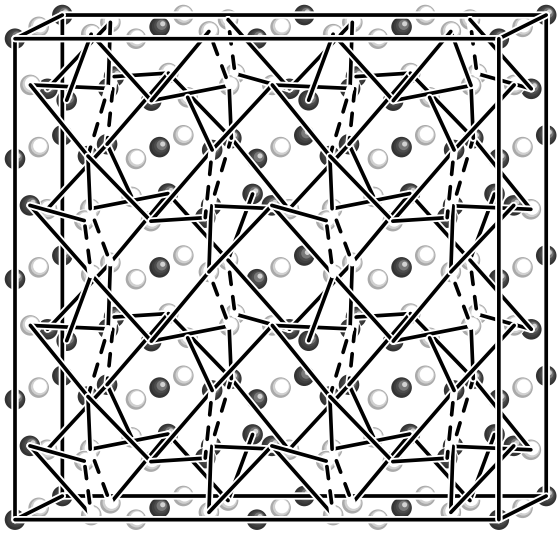

FIG. 14: Similar to Fig. 13, with the Mn-Mn pairs with the five strongest AFM interactions shown. One additional interaction, not shown in Fig. 13, is indicated by dotted lines here, and leads to frustrated triangles, which presumably is the origin of the noncollinear ground state magnetism.

The pair magnetic parameters, as determined from the fit to the DFT results, are shown as a function of Mn-Mn distance in Fig. 12. The strongest terms are antiferromagnetic terms for exactly those Mn-Mn pairs that (1) are approximately 3.5 Å to 3.6 Å apart, (2) share one close O atom bonded to each, and (3) have a Mn-O-Mn angle for these bonds less than 125°. These Mn-O-Mn pairs involve two Mn(3), Mn(4), or Mn(5) atoms and have very unequal Mn-O distances. Within the Mn-Mn pairs the magnitude of the antiferromagnetic interaction strictly decreases with increasing length of the longer Mn-O distance.

Aside from the Mn(1, 2)-Mn(1, 2) interaction at about 4.7 Å, which differs from zero by six standard deviations, all interactions beyond 4.0 Å are within about two standard deviations of zero. The calculated four-body terms are all within two standard deviations of zero, and only a single such term is more than one standard deviation away from zero. Note that negligible four-body interactions are deduced from the calculations rather than being assumed *a priori*. Conversely, by not assuming that all strong magnetic interactions are mediated by shared oxygen atoms, a significant interaction between Mn(1, 2)-Mn(1, 2) pairs at about 4.7 Å separation is discovered here.

Two pair interactions of approximate magnitude 0.085 eV per pair are nearly degenerate in energy and Mn-Mn distance, such that they can not be distinguished in Fig. 12. If the

Mn-Mn links corresponding to the 3 strongest terms and one of the 0.085 eV terms are drawn (Fig. 13), then the magnetic structure for the Mn(3), Mn(4), and Mn(5) sites based on these interactions, all antiferromagnetic, is completely determined to be that of the computational and experimental collinear ground state. On the other hand, if links corresponding to both 0.085 eV terms are drawn (Fig. 14), then there are frustrated triangles where antiferromagnetic interactions can not be satisfied for all bonds. A triangle of vector spins with frustrated antiferromagnetic interactions has a (possible degenerate) ground state with a noncollinear spin arrangement; we believe this is the origin of the noncollinear antiferromagnetism of α-Mn_2O_3.

We only looked at the ground state magnetic structure, but the finite temperature magnetic correlations could also be investigated using the DFT-based model, which would allow the nature of possible AFM-AFM transitions in α-Mn_2O_3 (6) to be determined.

Conclusions

First principles density functional theory DFT+U and cluster expansion model calculations, along with independent experimental neutron diffraction structure analyses, were used to determine the low-temperature crystallographic and magnetic structure of bixbyite α-Mn_2O_3. Both approaches independently gave nearly identical crystallographic and magnetic structures, with identical antiferromagnetic ordering along a principal magnetic axis and secondary ordering along a single orthogonal axis, differing only by a phase factor in the modulation patterns. The agreement between the two approaches suggests that the ground magnetic state of α-Mn_2O_3 is largely solved.

The computational methods exploited a Bayesian approach that allows the number of parameters in the cluster expansion model to exceed the number of input structure energies without sacrificing energy predictability. The individual magnetic coupling parameters were determined, showing that specific frustrated antiferromagnetic interactions determine the magnetic structure. The experimental approach benefited from optimized sample synthesis, which produced crystallite sizes large enough to yield a clear splitting of peaks in the neutron powder diffraction patterns, thereby enabling magnetic-structure refinements under the correct orthorhombic symmetry.

The approaches used here should prove suitable for similar problems of magnetic ordering

in other complex oxides whose magnetic states are determined by a large and frustrated set of antiferromagnetic interactions.

Acknowledgments

This work has benefited from the use of HIPD at the Lujan Center at Los Alamos Neutron Science Center, funded by DOE Office of Basic Energy Sciences. Los Alamos National Laboratory is operated by Los Alamos National Security LLC under DOE Contract DE-AC52-06NA25396.

---

[1] C. Franchini, R. Podloucky, J. Paier, M. Marsman, and G. Kresse, Phys. Rev. B **75**, 195128 (2007).

[2] K.-H. Hellwege and A. M. Hellwege, eds., *Landoldt-Börnstein Numerical Data and Functional Relationships in Science and Technology, Series III, Vol. 7.b.1* (Springer-Verlag, New York, 1975).

[3] S. Geller and G. P. Espinosa, Phys. Rev. B **1**, 3763 (1970).

[4] Table *b*1287 in the Landoldt-Börnstein volume cited (2) has the *b* and *c* parameters transposed with respect to the original Geller and Espinosa paper (3). Based on our results, we believe that the ordering in the original Geller and Espinosa work is correct for the standard *Pbca* space group setting.

[5] S. Geller, Acta Crystallogr. B **27**, 821 (1971).

[6] M. Regulski, R. Przenioslo, I. Sosnowska, D. Hohlwein, and R. Schneider, J. Alloys Compounds **362**, 236 (2004).

[7] R. W. Grant, S. Geller, J. A. Cape, and G. P. Espinoza, Phys. Rev. **175**, 686 (1968).

[8] G. Kresse and J. Furthmuller, Phys. Rev. B **54**, 11169 (1996).

[9] Certain commercial software is identified in this paper to adequately describe the methodology used. Such identification does not imply recommendation or endorsement by the National Institute of Standards and Technology, nor does it imply that the software identified is necessarily the best available for the purpose.

[10] J. P. Perdew, A. Ruzsinszky, G. I. Csonka, O. A. Vydrov, G. E. Scuseria, L. Constantin, X. Zhou, and K. Burke, Phys. Rev. Lett. **100**, 136406 (2008).

[11] G. I. Csonka, J. P. Perdew, A. Ruzsinszky, P. H. T. Philipsen, S. Lebègue, J. Paier, O. A. Vydrov, and J. G. Ángyán, Phys. Rev. B **79**, 155107 (2009).

[12] E. Cockayne and L. Li, Chem. Phys. Lett. **544**, 53 (2012).

[13] A. I. Liechtenstein, V. I. Anisimov, and J. Zaane, Phys. Rev. B **52**, R5467 (1995).

[14] A recent paper[25] on the manganite β-MnO_2 shows that the inclusion of both U and J parameters is required to reproduce the bandgap and the magnetic structure.

[15] J. M. Sanchez, F. Ducastelle, and D. Gratias, Physica A **128**, 334 (1984).

[16] J. M. Sanchez, Phys. Rev. B **81**, 224202 (2010).

[17] For clarity, cluster multiplicities due to symmetry are neglected in the text equations, but were properly weighted in the analysis.

[18] E. Cockayne and A. van de Walle, Phys. Rev. B **81**, 012104 (2010).

[19] E. T. Jaynes, *Probability Theory: The Logic of Science* (Cambridge University Press, Cambridge, U.K., 2003).

[20] A. Zunger, in *Statistics and Dynamics of Alloy Phase Transformations (NATO Adv. Sci. Inst. Ser. B, Physics 319)*, edited by P. E. A. Turchi and A. Gonis (Plenum Press, New York, 1994), pp. 361–419.

[21] A. C. Larson and R. B. V. Dreele, Tech. Rep. 86-748, Los Alamos National Laboratory, Los Alamos, NM (1994).

[22] A. S. Wills, Physica B **276**, 680 (2000).

[23] Although the lattice parameters resemble those of a tetragonal crystal, space group $Ia\bar{3}$ has no tetragonal subgroup; furthermore, we carefully examined the internal coordinates to verify that the structure is orthorhombic with space group *Pbca*.

[24] Neglect of four-body terms is justified because the total posterior spectra weight of the four-body terms is less than 0.001 that of the two-body terms; furthermore (see the Discussion), there is no evidence for statistically significant individual four-body terms.

[25] D. A. Tompsett, D. S. Middlemiss, and M. S. Islam, Phys. Rev. B **86**, 205126 (2012).